

# A new approach for constraining the Hubble constant from proper motions of radio jets.

Bartosz Lew<sup>1,3</sup>, Boudewijn F. Roukema<sup>1</sup>, Silke Britzen<sup>2</sup>, and Marcin P. Gawroński<sup>1</sup>

<sup>1</sup> Toruń Centre for Astronomy, Nicolaus Copernicus University, ul. Gagarina 11, 87-100 Toruń, POLAND

<sup>2</sup> Max-Planck-Institut für Radioastronomie, Auf dem Hügel 69, 53 121 Bonn, Germany

<sup>3</sup> National Astronomical Observatory, 2-21-1 Osawa, Mitaka, Tokyo 181-8588, Japan

7th February 2020

**Abstract** A new method for constraining the Hubble constant, based on proper motions and Inverse Compton Doppler factors of superluminally expanding jets, is presented. This approach relies on statistical Monte-Carlo simulations of the most probable viewing angle ( $\theta$ ) and the relativistic velocity of particles in a jet ( $\beta$ ). According to recent constraints on the density parameters  $\Omega_m = 0.27$  and  $\Omega_\Lambda = 0.73$ , a flat cosmological model is assumed. The value of the current Hubble constant is derived on basis of a sample of 234 jets from the VLBI CJF (Caltech-Jodrell Bank Flat-Spectrum) catalog of flat spectrum radio sources (Britzen et al. 2005c). Additional consistency checks have also been performed on specifically selected subsamples from the CJF catalog. We derive the probability distribution function of  $\beta$  ( $\varphi_\beta$ ) in order to derive a constraint on the most common velocity value of particles in jets in the sample,  $\beta_{fit} \approx 0.987$ . Using a Monte-Carlo method over various hypotheses on the intrinsic (but observationally unknown) distribution of the viewing angle  $\theta$ , we simulate an artificial Doppler factor distribution that reproduces the Doppler factor distribution inferred from observations, using the moving sphere model, and obtain the constraint on the most common viewing angle in our CJF sample,  $\theta \approx 9^\circ$ . The final Hubble constant value derived from these constraints is  $H_0 = 71 \pm 7$  km/s/Mpc .

**Key words.** cosmology: observations – cosmological parameters

## 1. Introduction

Attempts to use Active Galactic Nuclei (AGN) as a standard ruler to constrain cosmological parameters have a long history (e.g., Gurvits et al. (1998), Kellermann (1993) and references therein). Search for a distance measure independent of SNIa distance indicators is one of the strongest motivations. Homan and Wardle (Homan & Wardle 2000) have proposed a method of direct angular distance measurements to distant AGNs, relying on measured proper motions and estimated Doppler factors. They also marked consecutive implications for determining our local cosmology, provided there are sufficiently good constraints on the viewing angle and bulk motion. It has also been suggested, that local cosmological parameters (i.e. Hubble constant and deceleration parameter) can be constrained from observations of radio jets, propagating perpendicular to the line of sight (Pelletier & Roland 1989) or from motions and jet-counter-jet flux ratios (Taylor & Vermeulen 1997).

A great effort has been put into analytical considerations aiming at the quantization of number of processes that can possibly take place in expanding blobs of relativistic particles, ejected from centers of supermassive AGNs. These include modeling of spectral features and polarization of emitted radiation, processes of cooling, self-absorption, pair production, self up-scattering, radiation reprocessing etc. (Jones

et al. 1974; Ghisellini et al. 1993; Ghisellini 1987; Stawarz et al. 2004; Stern & Poutanen 2004; Mastichiadis & Kirk 1997). Great advances have been achieved in theoretical studies of the morphology, time evolution, and magnetic fields thanks to relativistic magnetohydrodynamical (RMHD) computer simulations e.g., Nishikawa et al. (1998, 1997); Koide et al. (1996). As for observations since the first detections of superluminal sources more than 30 years ago and repeating reports on new superluminal motions in distant AGNs, the resolution of VLBI experiments has improved, now reaching the level of tens of micro arcseconds, providing numerous data of cosmological importance (e.g. Vermeulen & Cohen (1994); Cohen et al. (1988); Jorstad et al. (2001); Pearson & Readhead (1981); Biretta et al. (1986); Zensus & Pearson (1988); Unwin et al. (1983, 1989); Wehrle et al. (1990); Ulvestad et al. (1981); Barthel et al. (1995, 1988); Pearson et al. (1987); Barthel et al. (1986); Pearson et al. (1986); Hough & Readhead (1987, 1988) and references therein).

In this paper, as in Homan & Wardle (2000), we compare the proper motions and intrinsic velocities of AGN jets in order to estimate the Hubble constant via angular distance measurements, using estimates of Doppler factors. However, we improve the precision by using Monte Carlo simulations in order to better understand the intrinsic distributions of velocities  $\beta$

and viewing angles  $\theta$ , and by using a new data set, that is a sub-sample of the complete CJF flat spectrum radio source catalog (Britzen et al. 2005c, 2005b; Taylor et al. 1996). The subset of this sub-sample with the highest quality proper motion estimates is also tested. The analysis utilizes the basic results of the Synchrotron Self-Compton model of emission (Jones et al. 1974; Ghisellini et al. 1993). The possibility of better inferring the constraints on the viewing angle by using a subset of objects with relatively high Doppler factors is also briefly investigated.

The paper is organized as follows. In section 2 the general idea of superluminal motion is introduced and basic formulas are derived. In section 3 theoretical considerations concerning the uncertainties of relevant quantities for constraining the Hubble constant and its uncertainty are presented. The final analysis of the uncertainties of  $H_0$  is presented in section 4. Our sample is discussed in section 5. The idea, method and the solution used to derive the Hubble constant are discussed in section 6. The final results, the discussion of this results in a broader context, and the conclusions are presented in sections 7, 8, and 9, respectively.

## 2. Apparent angular velocity

Imagine a jet moving at a velocity  $\beta = v/c$  at an angle  $\theta$  relative to the line of sight at some cosmological distance at redshift  $z$  (Fig. 1). Suppose that the jet emits a signal towards the observer O and let's denote this as an event 'A'. A second signal is then sent, denoted as an event 'B'. The time interval between the two events in the reference frame of the blob is  $\Delta t'$ . The

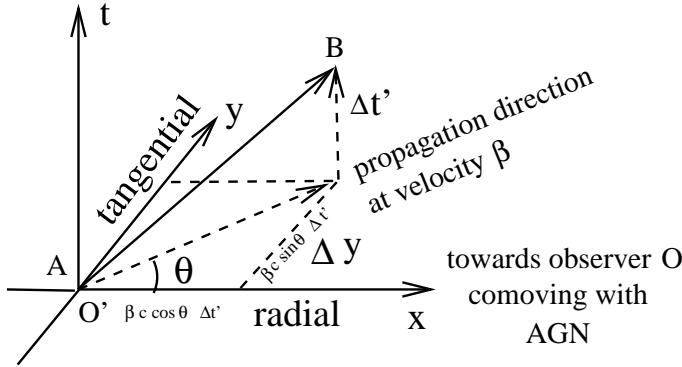


**Figure 1.** A jet blob, moving at velocity  $\beta$  in AGN's reference frame, is observed at two successive space-time events A and B.

apparent velocity of the expansion as seen by the observer O is

$$\beta^a = \frac{\beta \sin \theta \Delta t' / \gamma}{\Delta t}, \quad (1)$$

where  $\Delta t'$  corresponds to the time interval in O' reference frame and  $\Delta t$  corresponds to the time interval in O reference frame and  $\gamma$  is the Lorentz factor. Since the jet is moving at the relativistic velocity, it will cover a distance  $\beta c \cos \theta \Delta t'$  (in the co-moving reference frame) in time  $\Delta t'$ . Hence, the distance to the observer at the time when the second signal is sent, will be reduced by that amount. So the relation between the two time

intervals in the two reference frames (i.e. comoving with the AGN and comoving with the jet blob) will be:

$$\Delta t = \frac{1}{\gamma} \left( \Delta t' - \frac{\beta c \cos \theta \Delta t'}{c} \right) = \frac{\Delta t'}{\gamma} (1 - \beta \cos \theta), \quad (2)$$

Finally, from 1 and 2 we have

$$\beta^a = \frac{\beta \sin \theta}{(1 - \beta \cos \theta)(1 + z)} \quad (3)$$

where  $(1+z)$  factor is due to the conversion from comoving coordinates to physical coordinates. For future convenience we introduce

$$\Xi(\theta, \beta) \equiv \frac{\beta \sin \theta}{(1 - \beta \cos \theta)} \quad (4)$$

which is a term related only to the physical and geometrical features of a jet. Since only the changes in the position of blobs on the sky can be observed, it is necessary to express the Eq. 3 in terms of the observed angular velocity of the jet  $\dot{\phi}$ , where  $\Delta \phi$  is the measured angle by which the position of the jet has changed during the time interval  $\Delta t$  between two subsequent observations. In general  $\Delta \phi = S^a / d_A$ , where  $S^a$  is the apparent distance by which the jet has moved ( $\beta^a = \dot{S}^a / c$ ) and  $d_A$  is the angular size distance to the jet, thus

$$\dot{\phi} = \frac{1}{d_A^2} (\beta^a c d_A - \dot{d}_A S^a) \approx \frac{\beta^a c}{d_A} \quad (5)$$

since it is reasonable to assume that  $\dot{d}_A$  doesn't change much during  $\Delta t$ , the second term in the bracket in Eq. 5 can be neglected. From 3, 4 and 5 we obtain

$$\dot{\phi} = \frac{c}{d_A} \frac{\Xi(\theta, \beta)}{1 + z} = \frac{c}{d_{pm}} \Xi(\theta, \beta), \quad (6)$$

where  $d_{pm}$  is the proper motion distance to the jet.

$$d_{pm} = \lim_{r \rightarrow R_c} \left\{ r \cdot \text{sink} \left( \frac{d_p}{r} \right) \right\}, \quad (7)$$

where

$$d_p = \frac{c}{H_0} \int_0^z \frac{dz'}{E(z', \Omega_m, \Omega_\Lambda)}, \quad (8)$$

is the proper distance to the jet, the  $E$  factor is defined as in Peebles (1993), the  $\text{sink}(x) = \text{sink}(d_p/R_c)$  is

$$\text{sink}(x) = \begin{cases} \sinh(x), & k = -1 \\ x, & k = 0 \\ \sin(x), & k = 1 \end{cases}$$

and

$$R_c = \frac{c}{H_0} \cdot \frac{1}{\sqrt{1 - \Omega_m - \Omega_\Lambda}}, \quad (9)$$

is the curvature radius of the Universe.

To simplify the notation,  $\xi_m$  is assumed to be a dimensionless, model dependent value of the integral in Eq. 8.

$$\xi_m = \int_0^z \frac{dz'}{E(z', \Omega_m, \Omega_\Lambda)} \quad (10)$$

So, for the case  $k = 0$ , the Eq. 6 simplifies to

$$\dot{\phi} = H_0 \frac{\Xi(\theta, \beta)}{\xi_m} \quad (11)$$

In the remaining two cases the Eq. 6 cannot be solved for  $H_0$  analytically and should be discussed separately. However, since the Universe's curvature radius is constrained to be very large, ( $R_c \gtrsim 20\text{Gpc}$ ) its geometry is very close to flat (Spergel et al. 2003). We therefore concentrate on a discussion of the flat case.

For more analytical derivations of apparent superluminal motion see e.g. Chodorowski (2004).

### 3. $\Xi$ and $\xi_m$ factors analysis

It is important to constrain ranges of possible values for all factors that go into formula 11. In this section we estimate and present the uncertainties of  $\Xi$  and  $\xi_m$  factors respectively.

#### 3.1. Uncertainties of $\Xi$ factor

Fig. 2 shows  $\Xi$  as a function of jet inclination angle (jet viewing angle)  $\theta$  for increasing values of the blob velocity  $\beta$ .

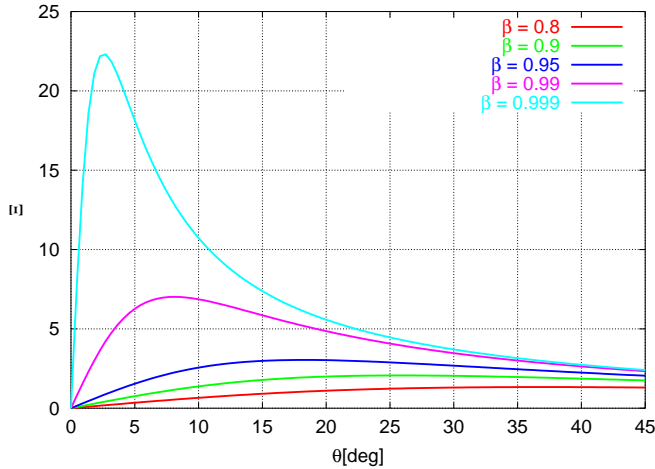


**Figure 2.** The maximum of each peak has value  $\beta\gamma$  (where  $\gamma = (1 - \beta^2)^{-1/2}$  is the standard Lorentz factor) and peaks at  $\theta^{max} = \arccos(\beta)$ . The maximum values of the different curves are 1.33, 2.06, 3.04, 7.02, and 22.3 and correspond to the following  $\beta$  values 0.8, 0.9, 0.95, 0.99, and 0.999 respectively.

The relations on Fig. 2 clearly show, that for a given viewing angle  $\theta$ , the value of  $\Xi$  factor rises with the linear speed of the blob. It is worth noting that, with increasing linear velocity  $\beta$ , the maximum value of  $\Xi$  factor shifts to smaller values of  $\theta$ , and the value itself grows very rapidly.

Since the final uncertainty of  $H_0$  strongly depends on the uncertainty of  $\Xi$  ( $\Delta\Xi$ ) and the relative error ( $\frac{\Delta\Xi}{\Xi}$ ) we will analyze theoretical uncertainties of this quantity. The  $\Xi$  factor is defined as in Eq. 4. Its uncertainty is

$$\Delta\Xi = \frac{|\sin(\theta)| \cdot \Delta\beta + \beta|\beta - \cos(\theta)| \cdot \Delta\theta}{(\beta \cdot \cos(\theta) - 1)^2} \quad (12)$$

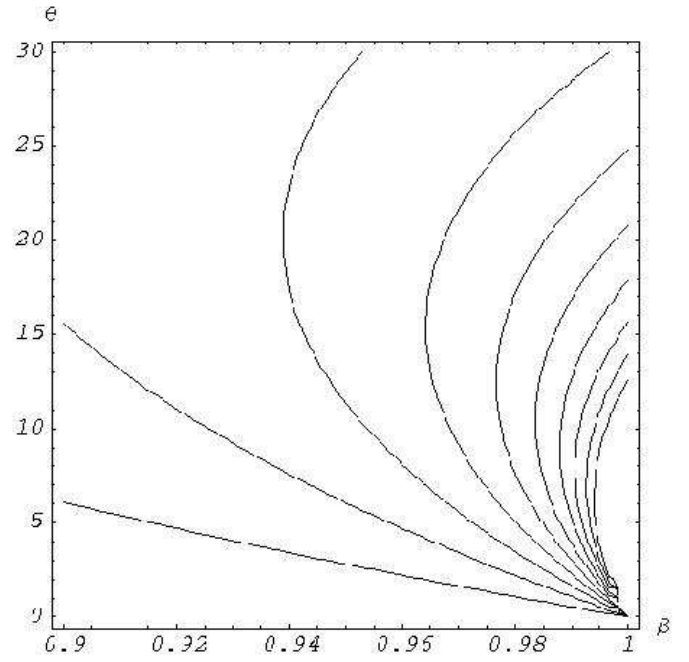


**Figure 3.** The relation from Eq.4. The ten consecutive contours are plotted within the range of  $\Xi$  between 0 and 10. Increasing trend of the value towards higher values of  $\beta$  and smaller inclination angles  $\theta$  (in degrees) is clearly seen.

and the relative error is:

$$\frac{\Delta\Xi}{\Xi} = \frac{\sin(\theta) \cdot \Delta\beta + |\beta \cdot \cos(\theta) - \beta^2| \cdot \Delta\theta}{[1 - \beta \cdot \cos(\theta)] \cdot \beta \sin(\theta)} \quad (13)$$

In order to quantify the sizes of uncertainties of  $\beta$  and  $\theta$ , we perform a separate analysis in terms of quantities that can be inferred directly from observations.

The Doppler (boosting) factor ( $\delta$ ) is defined as

$$\delta = \frac{1}{\gamma(1 - \beta \cos \theta)} = \frac{\sqrt{1 - \beta^2}}{1 - \beta \cos \theta}, \quad (14)$$

It is the factor by which the observed flux of a moving source is altered by collimation effects and the relative orientation of the observer. Its size can be inferred from spectral observations (Ghisellini et al. 1993) Eq.1, p.70. within an assumed physical model of the jet. We will try to derive constraints on ranges of possible values of  $\beta$  and  $\theta$  depending on a particular value of the Doppler factor.

In Fig. 4 the relation from Eq. 14 is plotted for all physically interesting ranges of  $\beta$  and  $\theta$ . (The most interesting range for  $\theta$  values is in fact from  $0^\circ$  to  $90^\circ$ , since for larger angles a jet becomes a counter-jet). The function is monotonic and rapidly growing for small inclination angles and relativistic velocities. From Figure 5 it can be easily seen, that the bigger Doppler factor is, the smaller is the uncertainty of both  $\beta$  and  $\theta$ , since the allowed region where  $\delta$  is still physically meaningful shrinks to zero. Provided an accurate Doppler factor value for a source is given, eq. (14) can be rewritten with the inclination angle  $\theta$  depending on the velocity of the particles in the jet  $\beta$  as follows:

$$\theta(\beta, \delta) = \frac{180^\circ}{\pi} \arccos\left(\frac{\delta - \sqrt{1 - \beta^2}}{\beta\delta}\right) \quad (15)$$

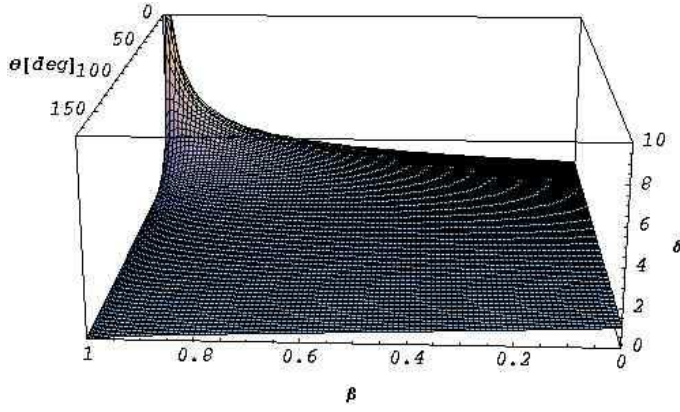


**Figure 4.** The dependence of Doppler factor ( $\delta$ ) with respect to  $\theta$  and  $\beta$ .

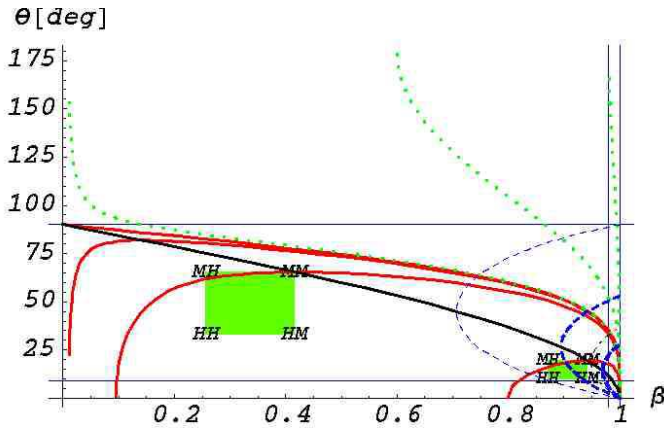


**Figure 5.** Allowed region of  $\theta$  and  $\beta$  variables given for increasing  $\delta$  values (the green (dotted) lines for  $\delta < 1$  and red (solid) lines for  $\delta \geq 1$ ). Larger  $\delta$  values produce smaller regions under the corresponding curve. The consecutive  $\delta$  values are: 0.1, 0.5, 0.99, 1.0, 1.01, 1.1, 3.0 respectively. The thick black line (running from  $(0, 90^\circ)$  to  $(1, 0^\circ)$ ) goes through all points that yield the maximum apparent expansion speed condition from the description of Fig. 2, i.e. it shows which angles maximize the apparent velocity for a given  $\beta$ . With dashed lines we present the behavior of apparent superluminal velocity. The blue (dashed) lines of increasing thickness show the contours of the same apparent velocity  $\beta^a \in \{1, 1, 2\}$  of a source at corresponding redshifts  $z \in \{0, 1, 1\}$ . The black (dot-dashed) line indicates the superluminality condition ( $\beta^a = 1$ ) for a source of redshift  $z = 2$ . See Eq. (22) for definitions of the characteristic points MH, MM, HH, HM. Thin horizontal lines show  $\theta = 90^\circ$  and  $\theta = 9^\circ$  — the latter is near the value for  $EX(\theta)$  found for the “MS” model in Sect. 6.2; a thin vertical line shows  $\beta = 0.98$ , near the value found in Eq. 32 for the “1st” quality data set in Sect. 6.1.

However the multi-wavelength spectral observations can only provide lower limits of the intrinsic Doppler factor. This corresponds to the whole region below the red lines for  $\delta > 1$  and green lines for  $\delta < 1$  in Fig. 5. In other words, every point taken as a combination of  $(\beta, \theta)$  from those regions can describe our source and define, introduced in Eq. 4, the  $\Xi$  quantity. It is in-

teresting to note that even in case of Doppler factors smaller than unity, the inclination angles still must always be smaller than  $90^\circ$ .

The inferred constraints are:

$$0 \leq \theta^\circ \leq \theta_{max} = \begin{cases} \frac{180^\circ}{\pi} \arccos\left(\frac{\sqrt{\delta^2-1}}{\delta}\right) & \delta \geq 1 \\ 90^\circ & \delta < 1, \end{cases} \quad (16)$$

where  $\theta_{max}$  is the maximal value of  $\theta$  for a given  $\delta$  and

$$\beta_{min}(\theta = 0^\circ) \leq \beta \leq \beta_+(\theta = 0^\circ) = 1, \quad (17)$$

where

$$\beta_{min}(\theta = 0^\circ) = \begin{cases} \beta_-(\theta = 0^\circ) = \frac{\delta^2-1}{\delta^2+1} & \delta > 1, \\ 0 & \delta < 1 \end{cases} \quad (18)$$

and

$$\beta_{\pm}(\theta, \delta) = \frac{\delta^2 \cos(\theta) \pm \sqrt{1 - \delta^2 + \delta^2 [\cos(\theta)]^2}}{1 + \delta^2 [\cos(\theta)]^2} \quad (19)$$

Fig. 6 presents derived  $\theta$  constraint (i.e. the value of  $\theta_{max}$  as a function of  $\delta$ ). As one can see,  $\theta_{max}$  is rapidly falling func-

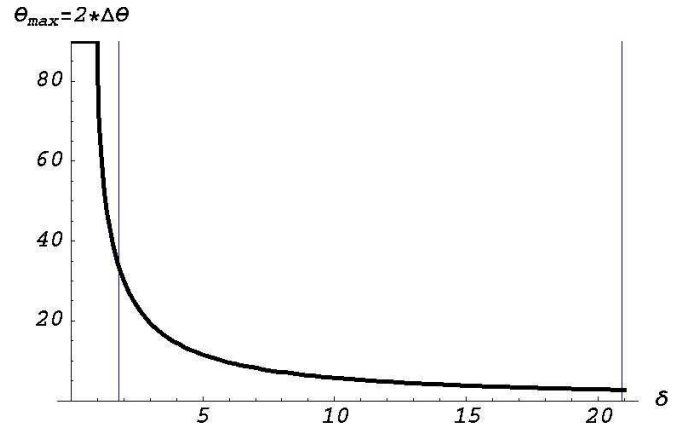


**Figure 6.** Constraint on  $\theta$  (in degrees) for some range of  $\delta$ .

tion of increasing  $\delta$ . In further calculations we conservatively assume, that the size of uncertainty for each source is half as big as the range given by the condition 16. Thus

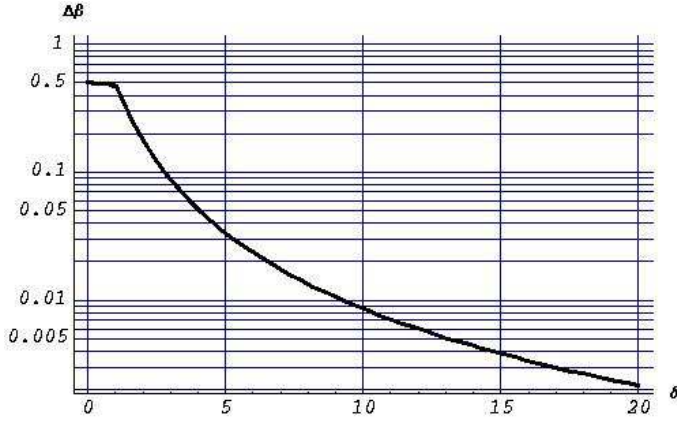
$$\Delta\theta \leq \theta_{max}/2 \quad (20)$$

As for the  $\beta$  uncertainty size, we assume it to be the half of the allowed range constrained by the eq. 15 for  $\theta = \theta_{max}/2$ . I.e.

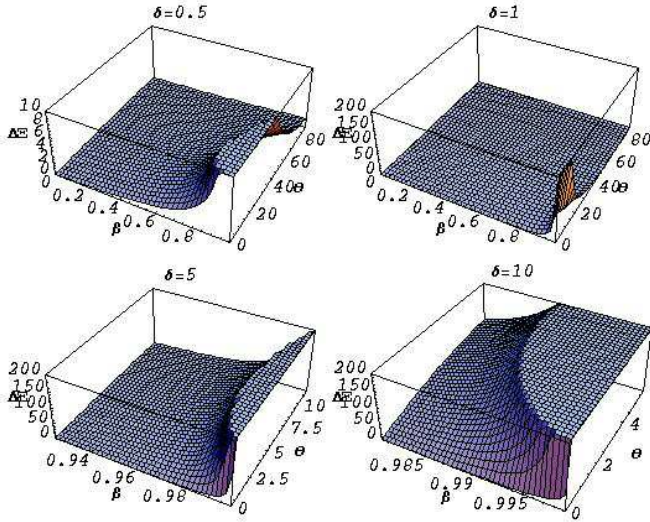
$$\Delta\beta = \left( \beta_+(\theta_{max}/2, \delta) - \beta_{min}(\theta_{max}/2, \delta) \right) / 2 \quad (21)$$

Fig. 7 shows derived  $\beta$  constraint as a function of  $\delta$ .

By substituting the derived constraints for the uncertainties of  $\theta$  and  $\beta$  into Eq. 12 and 13 we obtain a Doppler dependent relations for the uncertainties of  $\Xi$ . Plots on Fig. 8 and 9 show the magnitudes of the uncertainties for four different values of Doppler factor. Of course, Equations 12 and 13 are only valid for small errors, so in the regions where  $\frac{\Delta\Xi}{\Xi} \gtrsim 1$ , the “uncertainties” and “errors” that we refer to for  $\Xi$  are only



**Figure 7.** Constraint on  $\Delta\beta$  for some range of  $\delta$ .



**Figure 8.** The uncertainties of  $\Delta\Xi$  with respect to  $\beta$  and  $\theta$  (in degrees) for four increasing values of  $\delta$  parameter.

extrapolations, without a precise statistical meaning for individual estimates.

The plot range is chosen according to the constraints corresponding to the allowed values of the Doppler factor. Note, that the size of uncertainty significantly grows when approaching large values of  $\delta$  for both  $\Delta\Xi$  and  $\Delta\Xi/\Xi$ . According to the constraints (the possible values of  $\beta$  and  $\theta$ ) not all points in the area of the plots are possible. Only those values can be achieved, that lie within the region defined by the dividing line, corresponding to a particular Doppler factor, as shown in Fig. 5.

In order to show how these uncertainties depend on  $\delta$ , as an example, we now calculate them for four characteristic points in the  $\beta - \theta$  plane defined with aid of lower limits of the constraints defined in Eq. 16 and 17 and a point yielding the maximal apparent speed condition (the thick black line on Fig. 5). The four points hereafter called MM, HM, MH and HH are the

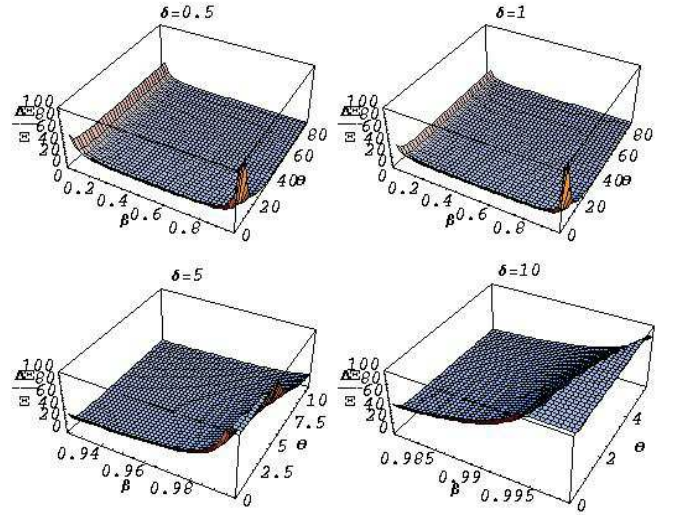


**Figure 9.** The uncertainties of  $\Delta\Xi/\Xi$  with respect to  $\beta$  and  $\theta$  (in degrees) for four increasing values of  $\delta$  parameter.

vertices of a rectangle and are defined as follows:

$$\begin{aligned}
 MM &= (\theta = \theta_{max}, \beta = \beta_{\pm}(\theta_{max}, \delta)) \\
 HM &= (\theta = \theta_{max}/2, \beta = \beta_{\pm}(\theta_{max}, \delta)) \\
 MH &= (\theta = \theta_{max}, \beta = (\beta_{\pm}(\theta_{max}, \delta) + \beta_{-}(0, \delta))/2) \\
 HH &= (\theta = \theta_{max}/2, \beta = (\beta_{\pm}(\theta_{max}, \delta) + \beta_{-}(0, \delta))/2)
 \end{aligned} \tag{22}$$

where

$$\beta(\theta_{max}) = \frac{\sqrt{\delta^2 - 1}}{\delta} \tag{23}$$

These points are named with regard to the position of a particular vertex, where the first letter is related to the  $\theta$  value, while the second to the  $\beta$  value. The 'M' and 'H' letters stand for maximal and half of maximal coordinate respectively for a given variable. The word "maximal" here is related to the maximal apparent velocity ( $\beta^a$ ) a jet can have, for a given either  $\beta$  or  $\theta$ . Two exemplary sets of these points are shown in Fig. 5, for two different values of  $\delta$  – 1.1 and 3 respectively. These points are only meaningful for  $\delta > 1$ , according to the constraints defined above.

The two sets of four plots on Fig. 10 show the theoretically derived values for  $\Delta\Xi$  and  $\Delta\Xi/\Xi$  at these points.

Clearly, the uncertainties of  $\Xi$  quantity rapidly grow, as higher values of the Doppler factor are approached. Therefore sources with relatively small  $\delta$ s are preferred.

### 3.2. Uncertainties of $\xi_m$ factor

Let us now analyze the size of the  $\xi_m$  uncertainty. For the calculations we assume a standard FLRW cosmology with flat geometry and density parameters consistent with recent WMAP results (Bennett et al. 2003) i.e.:

$$\begin{aligned}
 \Omega_m &= 0.27 \pm 0.04 \\
 \Omega_\Lambda &= 0.73 \pm 0.04
 \end{aligned} \tag{24}$$

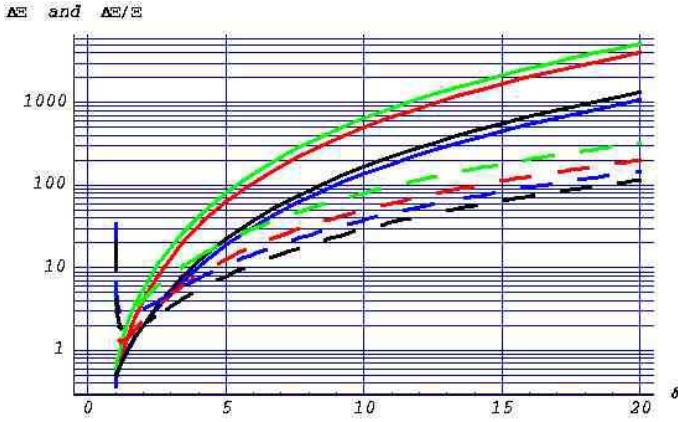


**Figure 10.** The dependence of  $\Delta \Xi$  (solid lines) and  $\frac{\Delta \Xi}{\Xi}$  (dashed lines) dependence on Doppler factor for four characteristic points on  $(\beta, \theta)$  plane from Fig. 5. The solid green, red, black and blue lines (from top to bottom) show the relations from Eq. 12 for the points HM, MM, MH and HH respectively. The dashed green, red, blue and black (from top to bottom) show the relations from Eq. 13 for the point HM, MM, HH and MH respectively.

Fig. 11 shows the derived values of  $\xi_m$  defined in Eq. 10. The two fitted, limiting lines (green and blue) define the maximal dispersion around the central values from Eq. 24.

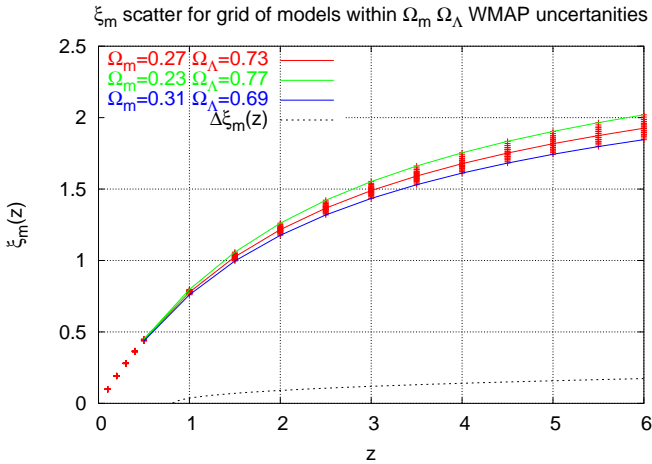


**Figure 11.** The dispersion of the  $\xi_m$  values for a two dimensional grid of models covering a range of values of parameters within the WMAP uncertainties from Eq. 24. The lower dashed line is the estimated size of  $\Delta \xi_m$ .

As shown in Fig. 11, the  $\xi_m$  values increase monotonically with redshift, since they represent increasing radial proper distances. Moreover, the dispersion around the central value also increases monotonically with redshift. Since the errors of the Hubble constant are directly proportional to  $\xi_m$  and its uncertainty, low redshift sources are naturally preferred. However, at low redshifts all cosmological effects (e.g. the expansion of the Universe) are smaller and are thus more likely biased by local conditions. For an av-

model vs. z	WMAP	$\Omega_m = 1, \Omega_\Lambda = 0$	$\Omega_m = 0.3, \Omega_\Lambda = 0$
1	$0.780 \pm 0.082$	0.59	0.65
2	$1.221 \pm 0.107$	0.85	0.99
3	$1.494 \pm 0.118$	1.00	1.21
4	$1.683 \pm 0.129$	1.11	1.37
5	$1.823 \pm 0.132$	1.18	1.48
6	$1.931 \pm 0.137$	1.24	1.58

**Table 1.** The derived values of  $\xi_m$  for different cosmological models and redshifts.

erage redshift in the biggest sample analyzed in this paper (i.e.  $z = 1.25$ ) the size of  $\xi_m$  uncertainty is  $\Delta \xi_m = 0.091$ . A good analytical fit to green and blue curves in a range of redshifts  $1 < z < 6$  gives formula  $\xi_m(z) = a \cdot (x + b)^c$  with set of  $\{a, b, c\}$  parameters  $\{1.020468, -0.757888, 0.313637\}$  and  $\{1.12053, -0.750238, 0.30307\}$  for green and blue curves respectively. The difference between them, representing the  $\xi_m$  uncertainty ( $\Delta \xi_m$ ) within the WMAP model is also plotted in Fig. 11 (the bottom, dashed line). The red line in the middle in Fig. 11 represents an average value of the two limiting lines.

Tab. 1 tabulates radial proper distances (in units of  $c/H_0 \approx 3h^{-1}$  Gpc) as a function of redshift. We conservatively adopt the WMAP model (the other models listed have lower uncertainties) for further calculations.

#### 4. Accuracy estimation for $H_0$

In this section we estimate the size of the uncertainty of  $H_0$  based on results from previous sections. For the flat case (from Eq. 11) we have

$$H_0 [\text{km/s/Mpc}] = \mu \frac{\dot{\phi} [\mu\text{as/yr}] \xi_m}{\Xi} \quad (25)$$

and the uncertainty is represented by three terms.

$$\Delta H_0 [\text{km/s/Mpc}] = \frac{\xi_m}{\Xi} \Delta [\mu\text{as/yr}] + \frac{\dot{\phi} [\mu\text{as/yr}]}{\Xi} \Delta \xi_m + \frac{\dot{\phi} [\mu\text{as/yr}] \xi_m}{\Xi^2} \Delta \Xi, \quad (26)$$

where  $\Delta$  is the uncertainty of  $\dot{\phi}$  and  $\mu = 4.7437$  is the conversion factor from mas/yr to km/s/Mpc. The statistical uncertainty for  $N$  sources should be smaller by a factor  $\sqrt{N}$  compared to Eq. 26, though, of course, for the  $\delta$  values with extremely large uncertainties, this is an extrapolation beyond the domain of conventional statistical models. In order to estimate the size of  $\Delta H_0$  we assume the following average values derived from one of the samples introduced later in this paper (see section 5).

$$\begin{aligned} \bar{\dot{\phi}} &= 120 \mu\text{as/yr} \\ \Delta &= 3.2 \mu\text{as/yr} \\ \xi_m(\bar{z} = 1.25) &= 0.86 \\ \Delta \xi_m(\bar{z} = 1.25) &= 0.091 \\ N &= 200 \end{aligned} \quad (27)$$

For the four points from Eq. 22 which define  $\Xi$  and  $\frac{\Delta \Xi}{\Xi}$  we estimate the uncertainties of the Hubble constant. The results are shown in Figs. 12 and 13. The two plots show the relations from

Eq. 26 as a function of  $\delta$ . The substantial difference is, that in the latter case (Fig. 13) the calculations include all terms from Eq. 26 (i.e it includes the results from Eq. 20 and 21). In the first case (Fig. 12) the uncertainties of  $\beta$  and  $\theta$  were assumed to be zero, which imply zero uncertainty for  $\Xi$ . This shows the *potential* precision which can be obtained if the uncertainties on  $\beta$  and  $\theta$  values can be made negligible. It can be easily seen in Fig. 13 that if  $\beta$  and  $\theta$  have non-negligible errors, then the  $H_0$  uncertainty *increases* for larger Doppler factors instead of decreasing. The growth is almost linear for all four characteristic points, which is a consequence of a rapid growth of the  $\frac{\Delta \Xi}{\Xi}$  function for small values of  $\theta$  and  $\beta$  values close to unity.

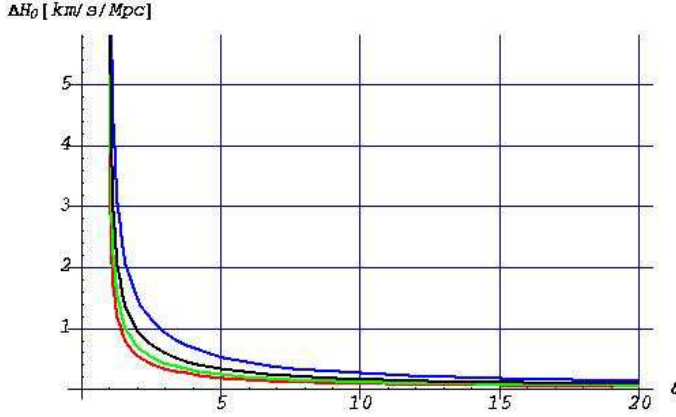


**Figure 12.** The dependence between the predicted Hubble constant uncertainty and the observed Doppler factor, for the four characteristic  $(\beta, \theta)$  points, MM, HM, MH, HH (from bottom to top) (Eq. 22). The prediction (for  $N = 200$  sources) is derived with the assumption that the viewing angle and the linear velocity of the particles in the jet are known ( $\Delta\beta = 0$ ,  $\Delta\theta = 0$ ).

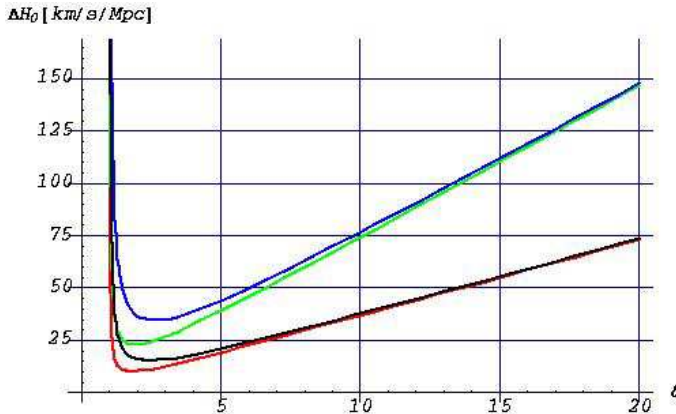


**Figure 13.** The relation between the predicted Hubble constant uncertainty and the observed Doppler factor, for the four characteristic  $(\beta, \theta)$  points, MM, MH, HM, HH (from bottom to top) (Eq. 22). The prediction (for  $N = 200$  sources) is derived assuming no constraints on the viewing angle and the linear velocity of the particles in the jet (Eq. 20 and 21).

We do not plot the errors for  $\delta < 1$  since for these values the definition of the chosen points (Eq. 22) is no longer reasonable. It is important to emphasize, that the actual values of  $\beta$  and  $\theta$  defined by points settled in terms of the limiting boundaries (like in Eq. 16 and 17) and implying a concrete  $\Xi$  value, depend on  $\delta$ . From a physical point of view, such approach of specifying at which point the Hubble constant is to be calculated is unnatural, because the velocity of emitting particles in a jet should be independent from the inclination angle of the jet. In this approach it is related through some measured value of Doppler factor. Our statistical method described in section 6 is free from these assumptions.

Summarizing the results, if there are priors on the inclination angle and the jet particles velocity, then the Hubble constant derivations will be most accurate when dealing with sources with the highest Doppler boosts. Plot 12 shows that the expected accuracy could be very promising. In case there are no priors on these quantities, there seems to be some preferred region in  $\delta$  space - i.e. the minimum in the plots on Fig. 13.

## 5. The Sample

We constrain the Hubble constant on the basis of data taken from the CJF catalog of 293 flat spectrum radio sources. For detailed discussion see (Britzen et al. 2005c, 2005b; Taylor et al. 1996). The data can generally be divided into two groups: “the first quality data” hereafter called “*Ist*” (containing 153 sources) and the complete catalog sample hereafter called “*all*” (containing 234 sources). The “*Ist*” is a sub-sample of “*all*” and is comprised of sources with most reliably well-defined proper motions based on VLBI studies (Britzen et al. 2005b). The Doppler factors in both samples were determined by combining radio with X-ray (ROSAT) measurements (Britzen et al. 2005a). In case of lack of X-ray detection of a source, a detection threshold was taken - i.e. the sensitivity limit for ROSAT satellite. For both samples, two Doppler factors were calculated, according to the two physical models of jets treated by formula 1 and 2 p.70 in Ghisellini et al. (1993). These are called “*MS*” and “*CJ*” which stand for ‘moving sphere’ and ‘continuous jet’ respectively. Ghisellini et al.’s relation between the two Doppler values is:

$$\delta_{CJ} = \delta_{MS}^{\frac{4+2\alpha}{3+2\alpha}} \quad (28)$$

where  $\alpha$  is the measured radio spectral index of a source. For details see Ghisellini et al. (1993) and references therein.

We have removed from the samples all sources with  $\delta > 100$ , for the sake of consistency with tabulated cumulative probability distribution functions (CPDF) presented in section 7 and also to avoid extreme values.

As an additional test we also utilize a sub-sample taken from “*Ist*” and “*all*” but with arbitrarily chosen values of minimal Doppler value cutoff. The cut threshold is set to 1 for the sample “*geq1*” (with 103 and 159 sources for “*Ist*” and “*all*” samples respectively) and 3 for the sample “*geq3*” (with 76 and 116 sources for “*Ist*” and “*all*” samples respectively). The results are briefly discussed in section 8.

Figures from 14 to 20 present the most relevant statistics obtained for the samples.

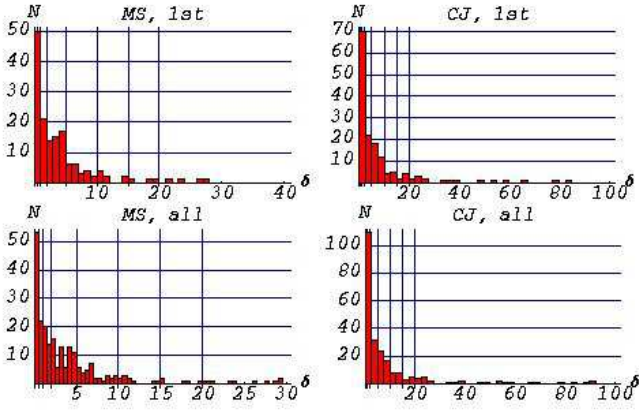


**Figure 14.** Doppler factor distribution for “1st” and “all” for “MS” and “CJ” cases.

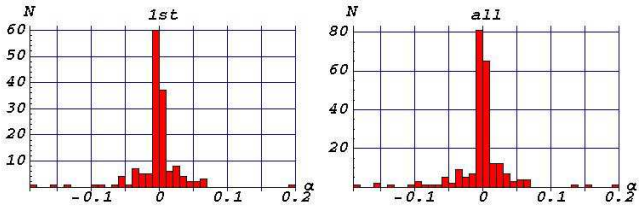


**Figure 15.** Spectral index distributions for “1st” and “all” samples.

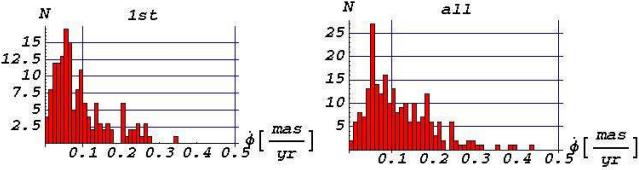


**Figure 16.** Proper motion distributions for “1st” and “all” samples.

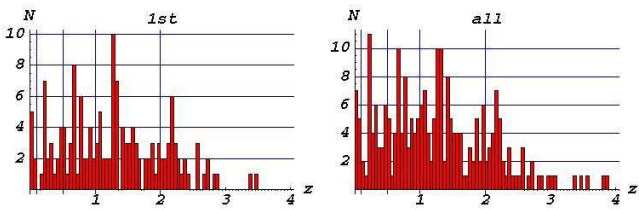


**Figure 17.** Redshift distributions for “1st” and “all” samples.

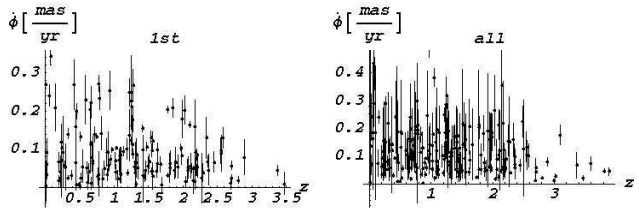


**Figure 18.** Proper motion-redshift relations for “1st” and “all” samples.

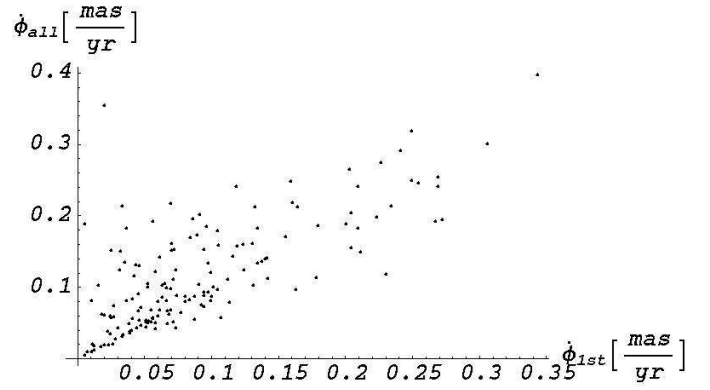


**Figure 19.** A comparison of proper motions for the sources which are present in both samples (“1st” and “all”). The plot directly shows slight differences in between the two samples.

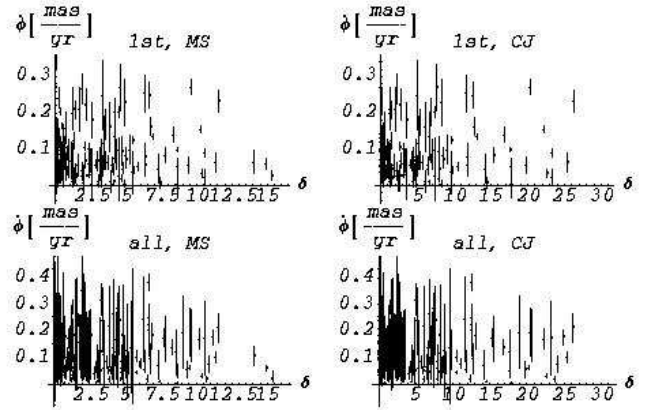


**Figure 20.** The proper motion-Doppler factor relations for “1st” and “all” samples for “MS” and “CJ” models.

## 6. The Method

In order to derive constraints for  $\beta$  and  $\theta$  parameters, we calculate probability distribution functions (PDF) and derive their expectancy values. Below we separately discuss the approach of constraining these parameters.

### 6.1. $\beta$ constraint

Because of the power law of the Lorentz factors ( $\gamma$ ) (e.g. section 3.1 Ghisellini et al. 1993) that is assumed in the jet models,

$$\varphi_\gamma = K\gamma^{-2\alpha-1} \quad (29)$$

(where  $K$  is the normalization factor) the corresponding PDF for  $\beta$  can be derived from equation

$$\varphi_\gamma d\gamma = \varphi_\beta d\beta \quad (30)$$

where  $\varphi$  is the PDF of a given quantity. The normalized PDF of  $\beta$  is therefore

$$\varphi_\beta^N = 2\alpha\beta(1-\beta^2)^{\alpha-1} \quad (31)$$

In Fig. 21 we present a set of  $\beta$  PDFs, for increasing values of the spectral index ( $\alpha$ ). It is clearly seen that the peak of the



distribution shifts to the lower values of the  $\beta$  as the spectrum gets steeper. However, since the CJF catalog is a catalog of flat spectrum sources, the big values of the spectral index are very rare and common values are close to zero.

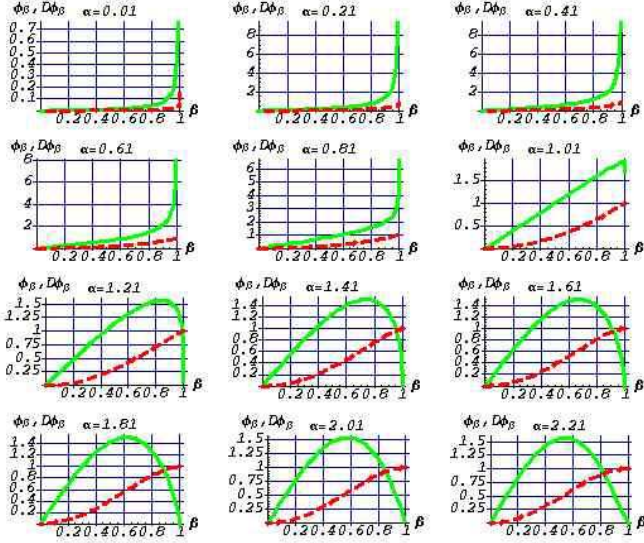


**Figure 21.**  $\beta$  PDFs for increasing values of spectral index (green/solid line). The cumulative probability functions of  $\beta$  PDFs are also plotted (red/dashed line).

The mean value  $\bar{\alpha}$  of  $\alpha$  values from all sources (for a given sample) with positive spectral indexes is calculated. The expectation value of the  $\beta$  PDF,  $EX\beta$ , is a function of  $\alpha$ , and is found by integration using  $\Gamma$  functions, followed by a fit with a fourth order polynomial. The  $\beta$  parameter constraint is the value of this polynomial fit (to  $EX\beta$ ) with the spectral index set to  $\bar{\alpha}$ . Figure 22 shows derived expectancy values for different values of the average (positive) spectral indexes.

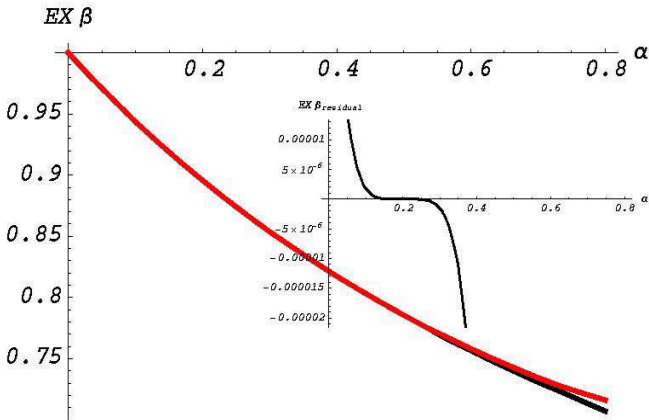


**Figure 22.**  $EX\beta$  values are shown as a function of the average positive spectral index value. In addition, the fourth order polynomial fit to  $EX\beta$  as a function of  $\alpha$  (red line) and the residual values (small plot) between the  $EX\beta$  and its fit are plotted.

Below we summarize the  $\beta$  constraints used for  $H_0$  calculation for each sample.

$$\begin{aligned} \bar{\beta}^{\text{“1st”}} &= 0.980856, \quad \bar{\alpha} = 0.032033 \\ \bar{\beta}^{\text{“all”}} &= 0.987296, \quad \bar{\alpha} = 0.021024 \end{aligned} \quad (32)$$

## 6.2. $\theta$ constraint

The  $\theta$  constraint is derived as the expectancy value of the  $\theta$  PDF ( $\varphi_\theta$ ). The PDF is selected as the best fit to the observed Doppler factors distribution of an artificially, randomly generated sample, parametrized by parameters representing the distribution of viewing angles  $\theta$  and that yields the derived  $\delta$  distribution function ( $\varphi_\delta$ ). A search for the best fit to the observed Doppler distribution ( $\varphi_\delta^{\text{CJF}}$ , for the CJF catalog) gives the most common and thus the most preferred viewing angle for all sources in the sample. In other words, we assume that the distribution of sources in our sample in  $\theta$  space is not uniform, i.e. that there is some preferred inclination angle for the selected sources. The  $\theta$  distribution is assumed to be Gaussian-like and is parametrized to form a grid of distributions. These distributions along with the  $\beta$  PDF imply a distinctive Doppler factor distribution which can be compared to the observed one for example in terms of specifically chosen distribution moments (like average value, skewness, kurtosis etc.). The PDF function of  $\delta$  can be calculated from:

$$\varphi_\delta^{\mathbf{q}}(\delta) = \frac{\partial D_{\varphi_\delta}^{\mathbf{q}}(\delta)}{\partial \delta} \quad (33)$$

where  $D_{\varphi_\delta}^{\mathbf{q}}(\delta)$  is the cumulative distribution function (CPDF) of  $\delta$  PDF defined by

$$D_{\varphi_\delta}^{\mathbf{q}}(\delta) = \int_0^1 \varphi_\beta(\bar{\alpha}, \beta) \int_{\theta_l(\beta, \delta)}^{\theta_u(\beta, \delta)} \varphi_\theta(\mathbf{p}, \theta) d\theta d\beta \quad (34)$$

and parametrized by  $\mathbf{q} = (\bar{\alpha}, \mathbf{p})$ , where

$$\varphi_\theta(\mathbf{p}, \theta) = \frac{1}{\sqrt{2\pi}\sigma} \exp\left(-\frac{(\theta - \theta_{max})^n}{2\sigma^2}\right) \quad (35)$$

is the assumed, Gaussian-like PDF of  $\theta$ , parametrized by  $\mathbf{p} = (\theta_{max}, \sigma, n)$  and the  $\theta$  integration limits are defined by:

$$\theta_l(\beta, \delta) = \begin{cases} \theta(\beta, \delta), & \theta(\beta, \delta) \leq 90^\circ \\ 90, & \theta(\beta, \delta) > 90^\circ \end{cases} \quad (36)$$

where  $\theta(\beta, \delta)$  is defined in Eq. 15. The index  $n$  is  $n = 2$  for a Gaussian PDF and  $n = 4$  for a narrower, somewhat Gaussian-like PDF. The  $\delta_{th}$  (upper limit in the inside integration of Eq. (34)) is the minimal Doppler factor value cutoff. In CPDF calculations with no forced priors on minimal Doppler factor this value is set to  $\delta_{th} = 0.01$ . In case of “*geq1*” and “*geq3*” samples it’s set to 1 and 3 respectively.

The  $\bar{\alpha}$  value for each sample is the value listed in Eq. 32.

In order to find the best fitting model of  $\theta$  PDF we perform a  $\chi^2$  tests on a grid of 108 different  $D_{\varphi_\delta}^{\mathbf{q}}$  models of  $\delta$  distribution in the following parameters grid.

$$\begin{aligned} \theta_{max} [^\circ] &= \{2, 4, 6, 8, 10, 15, 30, 60, 90\} \\ \sigma &= \{1, 2, 4, 8, 16, 32\} \\ n &= \{2, 4\} \end{aligned} \quad (37)$$

Each randomly generated sample of  $\delta$  with derived PDF is described by three estimators, which are next compared with the corresponding estimators in the sample from CJF catalog. These are: an average value of the Doppler distribution ( $\bar{\delta}$ ), skewness ( $S$ ) and kurtosis ( $K$ ). The best fit model is found by minimizing

$$\chi^2 = \sum_{i=1}^M (\bar{\delta}_i - \bar{\delta}_{CJF})^2 + (S_i - S_{CJF})^2 + (K_i - K_{CJF})^2 \quad (38)$$

where  $M$  denotes the number of randomly generated distributions within one particular model of  $D_{\varphi_\delta}^q$ .

Once the model that reproduces the observed Doppler factor distribution is found, the corresponding  $\varphi_\theta$  model, normalized within ( $0^\circ$ ,  $90^\circ$ ) range, is taken and its expectancy value  $EX(\theta)$  is calculated with an accurate value of the  $\mathbf{p}$  parameter vector. When Hubble constant estimates are made in the following section, individually for each source, this  $EX(\theta)$  value is used as the  $\theta$  estimate.

### 6.3. $H_0$ constraint

For each source, by default, we use Eq. (25) to calculate  $H_0$  for that source using the  $\bar{\beta}$  estimate from Eq. (32), the  $EX(\theta)$  estimate as described in the previous section, the observed proper motion  $\dot{\phi}$ , and the WMAP ( $\Omega_\Lambda$ ,  $\Omega_m$ ) values.

It is possible, that for a source with sufficiently big  $\delta$  value, the point estimated for the full sample ( $\bar{\beta}$ ,  $EX(\theta)$ ) may out stand beyond the allowed region below the line defined in Eq. 15. In such cases, if ( $\bar{\beta}$ ,  $EX(\theta)$ ) lies outside the region (defined by the  $\delta$  value for the source) in the  $\theta$  direction, then the biggest allowed  $\theta$  value is taken at given  $\bar{\beta}$  instead of  $EX(\theta)$ . If the pair ( $\bar{\beta}$ ,  $\theta$ ) still lies outside the region in the  $\beta$  direction, then the source is not included in further calculations.

The final Hubble constant value is the mean of all individually calculated values for all sources in a sample, excluding those with invalid  $\beta$  values.

As a control test of the method, we also perform random realizations of Doppler distributions for a flat  $\theta$  PDF. It is done in order to find out whether the best matching  $\theta$  distribution is indeed more suitable then the uniform  $\theta$  distribution.

Fig. 25 shows a random realization of Doppler distribution assuming a flat model for  $\varphi_\theta$ .

We also perform a high precision, two-stage calculations of  $D_{\varphi_\delta}^q$  function for smaller nonlinear grids. First one is:

$$\begin{aligned} \theta &= \{4, 8, 15, 30, 60\} \\ \sigma &= \{2, 8, 16, 32\} \\ n &= \{2\} \end{aligned} \quad (39)$$

and then the second, much denser grid is set around a place preselected by primary tests. The second grid is:

$$\begin{aligned} \theta &= \{7, 8, 9, 10, 11\} \\ \sigma &= \{2, 8, 16, 32\} \\ n &= \{2, 4\} \end{aligned} \quad (40)$$

For future convenience we name the first grid “*grid108*”, the second grid “*grid20*” and the third grid “*grid40*”, after the number of models covered by each of them.

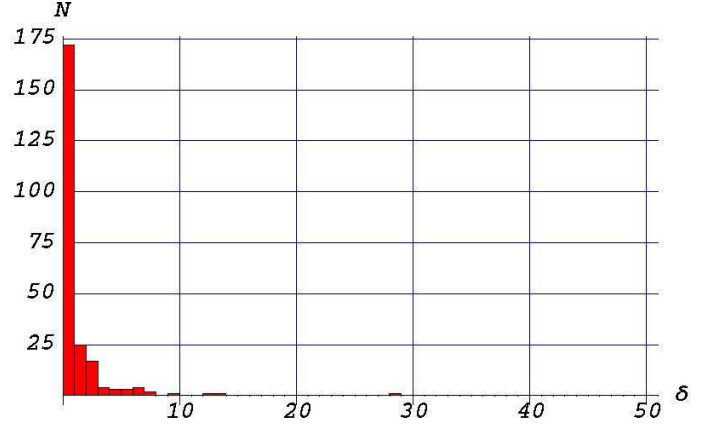


**Figure 25.** Random  $D_{\varphi_\delta}^q$  function realization with assumption of flat  $\varphi_\theta$  model. The number of generated sources (234) corresponds to the “*all*” sample. Notice that this particular realization seems to be much steeper than the observed one.

An example of one random realization of all 20+40 models (from “*grid20*” and “*grid40*” respectively) from the  $D_{\varphi_\delta}^q$  function with 10 000 generated sources in each is shown in Figs. 23 and 24. Within the same inclination angle  $\theta$  and ‘kurtosis’ coefficient ‘ $n$ ’ subsequent realizations of the  $D_{\varphi_\delta}^q$  functions for increasing  $\sigma$  gradually, and monotonically shift the peak of the distribution towards lower values of  $\delta$ , making also each next distribution steeper than the last.

## 7. Results

We have calculated the cumulative probability functions ( $D_{\varphi_\delta}^q$ ) for all grids described in section 6, for the two models (CJ and MS) and the flat  $\theta$  PDF cases. Figures 26, 27 and 28 show the results of the calculations for all grids.

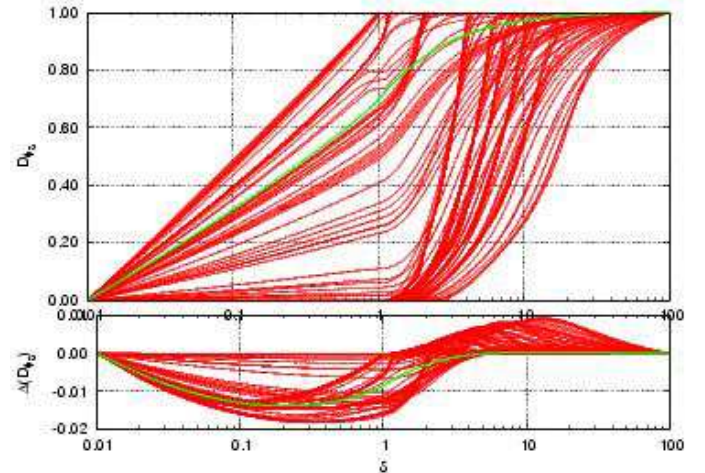


**Figure 26.**  $D_{\varphi_\delta}^q$  functions for all models in “*grid108*” for sample “*1st*” (top panel) and the differences between the “*1st*” and “*all*” samples for “*grid108*” and the flat cases (bottom panel). Note, that some of the models have a sort of a kink. These little features are caused only by the computational effect of finite accuracy applied in calculations. The green (gray) line indicates the flat  $\theta$  distribution case.

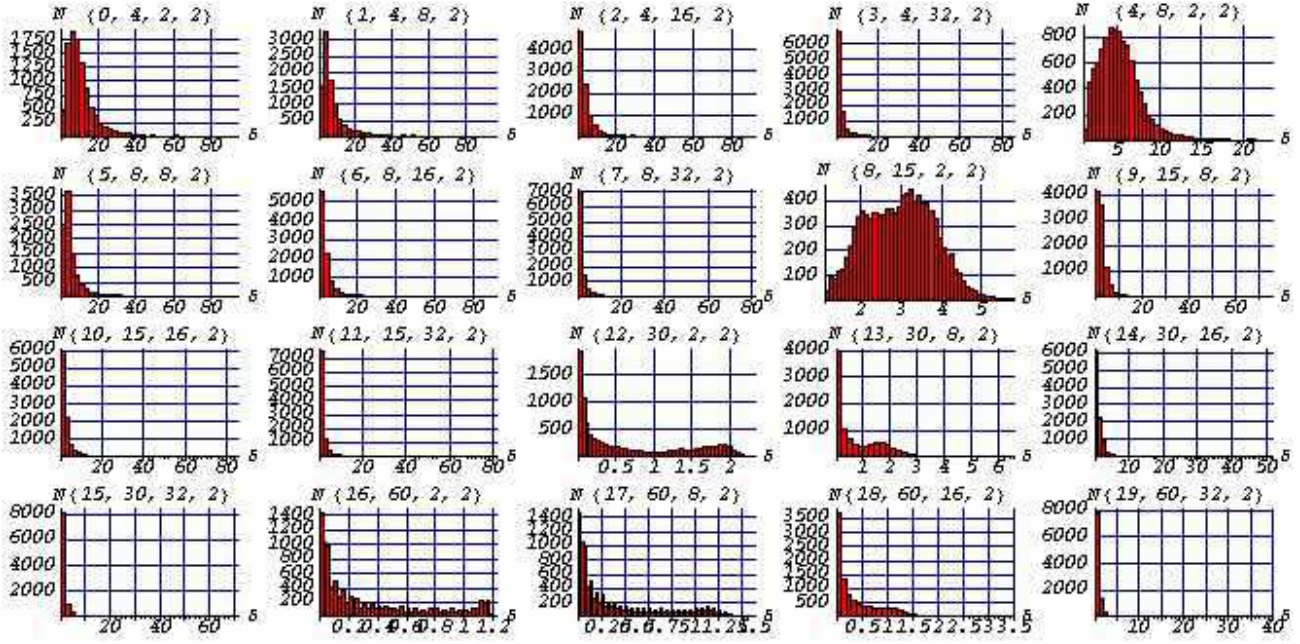


**Figure 23.** Random  $D_{\varphi_s}^q$  function realization for 20 models from “grid20” with 10 000 sources generated in each. The distributions were calculated for sample “1st” according to Eq. 32. Above each plot the corresponding plot number and  $\mathbf{p}$  parameter is

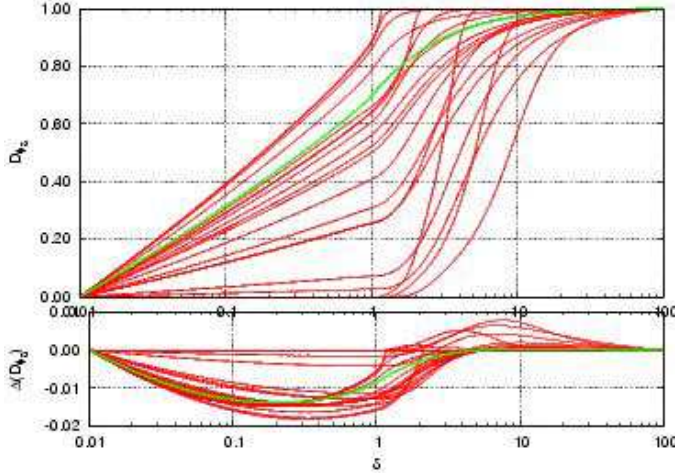


**Figure 27.**  $D_{\varphi_s}^q$  functions for all models in “grid20” for sample “1st” (top panel) and the differences between the “1st” and “all” samples for “grid20” and the flat cases (bottom panel). The green (gray) line indicates the flat model case.

We performed random Monte-Carlo realizations for all 108  $D_{\varphi_s}^q$  models plus the flat model case for each series of tests for each sample. Table 2 summarizes the results from all tests and all samples considered in this paper for “grid108”. The table contains the Hubble constant values derived for the priors on  $\beta$  (according to Eq. 32) and  $\theta$ . In square brackets the corresponding  $\mathbf{p}$  parameter along with  $\theta$  PDF expectancy value is given. In round brackets we give the number of sources from which a particular value was calculated.

We also perform another set of tests on the two remaining grids. Table 3 summarizes the results.

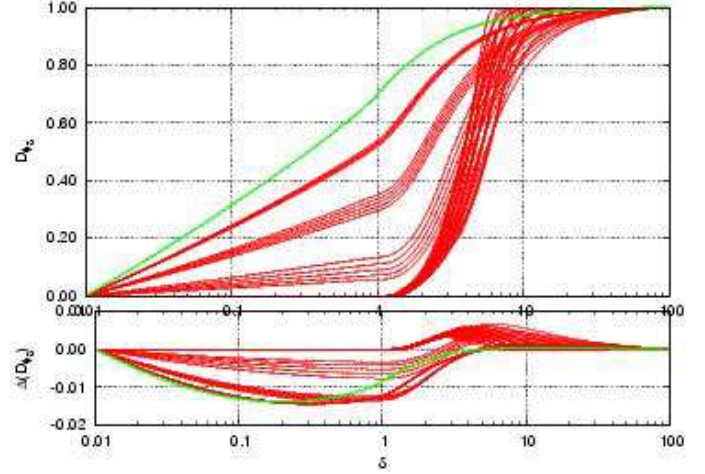


**Figure 28.**  $D_{\varphi_s}^q$  functions for all models in “grid40” for sample “1st” (top panel) and the differences between the “1st” and “all” samples for “grid40” and the flat cases (bottom panel). The green (gray) line indicates the flat model case.

In Fig. 29 we present an example of results of  $\chi^2$  tests, to show the dispersion resulting from different models in the grid.

The final value of the Hubble constant, constrained from the most precise grid (“grid40”) and calculated as an overall average from both samples from table 3 is:

$$H_0 = 71 \pm 7 \text{ km/s/Mpc} \quad (41)$$

where the uncertainty is calculated as described in Sections 3 and 4.

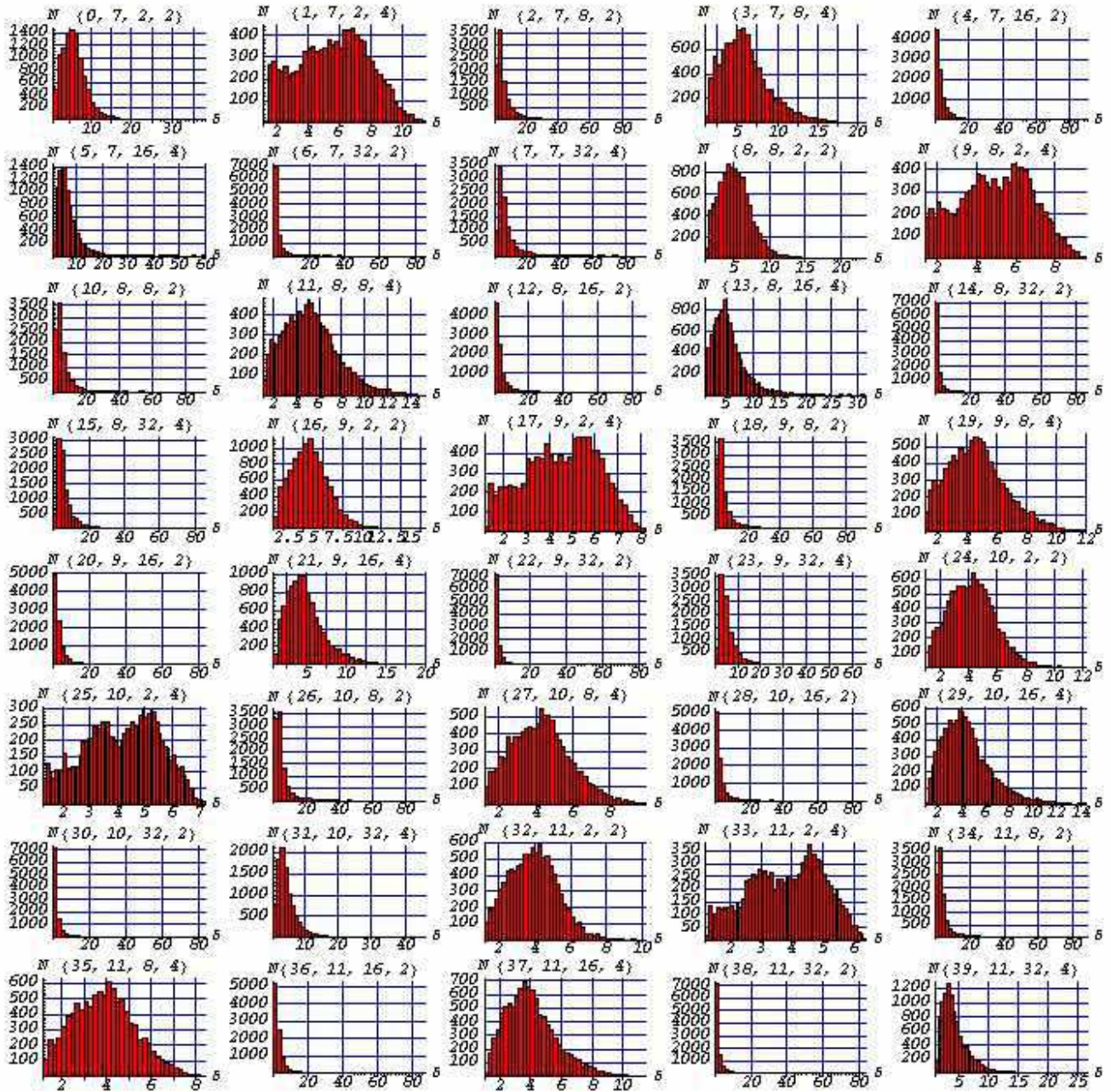


**Figure 24.** Random  $D_{\varphi\sigma}^q$  function realization for 40 models from “grid40” with 10 000 sources generated in each. The distributions were calculated for sample “1st” according to Eq. 32. Above each plot the corresponding plot number and  $\mathbf{p}$  parameter is given ( $\theta, \sigma, n$  respectively).

		“grid108”			
sample/test		N=1000, M=10	N=1000, M=100	N=10000, M=1	N=10000, M=10
“1st”	MS	$75 \pm 7$ (132)	$75 \pm 7$ (132)	$75 \pm 7$ (132)	$75 \pm 7$ (132)
	CJ	$\{[8, 2, 2], EX\theta = 8.0^\circ\}$ $104 \pm 11$ (120)	$\{[8, 2, 2], EX\theta = 8.0^\circ\}$ $100 \pm 10$ (120)	$\{[8, 2, 2], EX\theta = 8.0^\circ\}$ $104 \pm 11$ (120)	$\{[8, 2, 2], EX\theta = 8.0^\circ\}$ $105 \pm 11$ (120)
“all”	MS	$72 \pm 10$ (204)	$78 \pm 11$ (208)	$72 \pm 10$ (204)	$72 \pm 10$ (204)
	CJ	$\{[8, 2, 2], EX\theta = 8.0^\circ\}$ $95 \pm 15$ (184)	$\{[6, 8, 4], EX\theta = 6.0^\circ\}$ $95 \pm 15$ (184)	$\{[8, 2, 2], EX\theta = 8.0^\circ\}$ $95 \pm 15$ (184)	$\{[8, 2, 2], EX\theta = 8.0^\circ\}$ $95 \pm 15$ (184)
		$\{[2, 4, 2], EX\theta = 4.03^\circ\}$	$\{[2, 4, 2], EX\theta = 4.03^\circ\}$	$\{[2, 4, 2], EX\theta = 4.03^\circ\}$	$\{[2, 4, 2], EX\theta = 4.03^\circ\}$

**Table 2.** The results of the Monte Carlo simulations. The Hubble constant values are provided in km/s/Mpc. N denotes the number of sources generated in each test for “grid108”.

		"grid20"			
sample/test		N=1000, M=10	N=1000, M=100	N=10000, M=1	N=10000, M=10
"1st"	MS	75 ± 7 (132) [8, 2, 2], EXθ = 8.0°	75 ± 7 (132) [8, 2, 2], EXθ = 8.0°	75 ± 7 (132) [8, 2, 2], EXθ = 8.0°	75 ± 7 (132) [8, 2, 2], EXθ = 8.0°
	CJ	70 ± 7 (112) [8, 2, 2], EXθ = 8.0°	103 ± 10 (120) [4, 2, 2], EXθ = 4.11°	70 ± 7 (112) [8, 2, 2], EXθ = 8.0°	103 ± 10 (120) [4, 2, 2], EXθ = 4.11°
"all"	MS	72 ± 10 (204) [8, 2, 2], EXθ = 8.0°	72 ± 10 (204) [8, 2, 2], EXθ = 8.0°	72 ± 10 (204) [8, 2, 2], EXθ = 8.0°	72 ± 10 (204) [8, 2, 2], EXθ = 8.0°
	CJ	72 ± 12 (170) [8, 2, 2], EXθ = 8.0°	94 ± 15 (184) [4, 2, 2], EXθ = 4.11°	72 ± 12 (170) [8, 2, 2], EXθ = 8.0°	94 ± 15 (184) [4, 2, 2], EXθ = 4.11°
		"grid40"			
"1st"	MS	70 ± 7 (127) [9, 16, 4], EXθ = 9.0°	70 ± 7 (127) [9, 16, 4], EXθ = 9.0°	75 ± 7 (132) [8, 2, 2], EXθ = 8.0°	70 ± 7 (127) [9, 16, 4], EXθ = 9.0°
	CJ	73 ± 7 (113) [7, 2, 2], EXθ = 7.0°	70 ± 7 (112) [8, 16, 4], EXθ = 8.0°	70 ± 7 (113) [7, 2, 2], EXθ = 7.0°	70 ± 8 (112) [8, 16, 4], EXθ = 8.0°
"all"	MS	70 ± 10 (200) [9, 16, 4], EXθ = 9.0°	70 ± 10 (200) [9, 16, 4], EXθ = 9.0°	72 ± 10 (204) [8, 2, 2], EXθ = 8.0°	70 ± 10 (200) [9, 16, 4], EXθ = 9.0°
	CJ	72 ± 12 (170) [8, 16, 4], EXθ = 8.0°	72 ± 12 (170) [8, 16, 4], EXθ = 8.0°	72 ± 12 (170) [8, 16, 4], EXθ = 8.0°	72 ± 12 (170) [8, 16, 4], EXθ = 8.0°
average	MS	70 ± 6	70 ± 6	74 ± 6	70 ± 6
all:	CJ	73 ± 7	71 ± 7	73 ± 7	71 ± 7

**Table 3.** The results of the Monte Carlo simulations. The Hubble constant values are provided in km/s/Mpc. N denotes the number of sources generated in each test for "grid20" and "grid40".

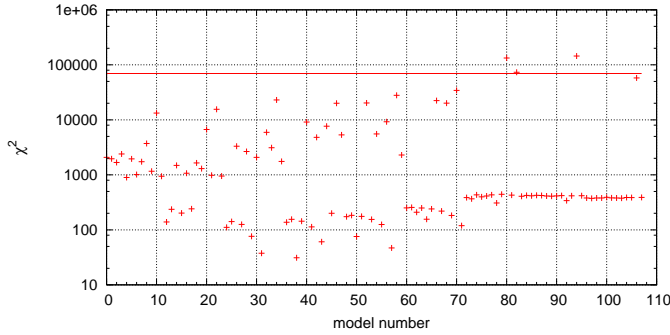


**Figure 29.** The results of  $\chi^2$  tests for ten realizations of the  $D_{\phi_\delta}^\alpha$  function for "grid108" with 1000 generated sources in each. These results are based on the sample "all". Only "MS" case is plotted. The horizontal line shows a control test for 10 flat model realizations with the same number of sources.

## 8. Discussion

The results, over a wide range in  $\theta$  values, shown in Table 2, generally concentrate around two different values of the Hubble constant. These values correspond strictly to the jet model (a low Hubble constant for the MS model and a high Hubble constant for the CJ model), via the  $\theta$  estimate for the sample. However, focusing on the  $EX(\theta)$  values selected in calculations with "grid108" leads to the results presented in Table 3. The degeneracy (double solution) in Hubble constant values also occurs for the simulations shown in "grid20" for the higher values of  $M$ , i.e. where larger numbers of simulations are run.

In "grid40", the  $EX(\theta) \approx 4.0^\circ$  solution (see Eq. 40) favoured by the CJ model is removed from the region of parameter space explored, and in this case the CJ model yields similar solutions to the MS model.

The single value approximation of viewing angles in a population of sources was introduced because the sources have generally flat spectrum and are mostly of the same observational type. The assumption of narrow, nonuniform distribution of inclination angles might be expected from spiky distribution of the spectral indexes (Fig. 15) of the sources from our samples introduced in section 5. These are the subsamples of the CJF flat spectrum radio source catalog. The single  $\theta$  value

approximation of the unknown, intrinsic distribution of inclination angles of sources in our samples, statistically becomes more accurate, when the distribution is more compactly centered on that particular  $\theta$  (i.e.  $EX(\theta)$ ) value. Therefore, although introducing some restrictive source type selection criteria, generally results in smaller samples, it might help prevent introducing wide  $\theta$  distribution, thus making the approximation more accurate. The large tail in the inferred  $H_0$  distribution (Fig. 30) is probably due to the fact, that the estimated individual Hubble constant values are highly sensitive to small variations in the inclination angle (which in this paper is approximated for the whole sample), especially in the regime of small inclination angles and large  $\beta$  values.

The method of finding the best viewing angle for whole population of sources in the sample, generally does have some dependence on the threshold for minimum Doppler values cut-off. It is important to emphasize that a population of sources with corresponding Doppler factors distributed from zero to some maximal value does not necessarily have a uniformly populated  $\theta$  space. Small values of Doppler factors can easily be obtained with highly relativistic jets (having small opening angle in which they emit most of the collimated radiation) but being observed from relatively large viewing angles (see Fig. 31). Thus, although we consider a broad range of possible Doppler factors in the "all" sample, it is still very possible for the sources to congregate along a certain value of inclination angle. On the other hand, introducing some minimal Doppler value cut into a sample (e.g. "geq3") for the majority of sources in the sample this means, that the observed Doppler factor value, for sources seen under a certain angle (which is in this case much better constrained as shown in Fig. 5) will always be smaller, for smaller  $\beta$  values, than for sources with bigger  $\beta$  values (Fig. 4). Provided that generally jets are highly relativistic, such operation (i.e. introducing some arbitrary Doppler cutoff) forces tight constraints on  $\theta$  angle. However, the number of sources yielding such a prior is smaller, and it may happen, that it will not be possible to derive  $H_0$  because of lack of sources fitting into allowed  $\beta - \theta$  region, or lack of proper statistics.

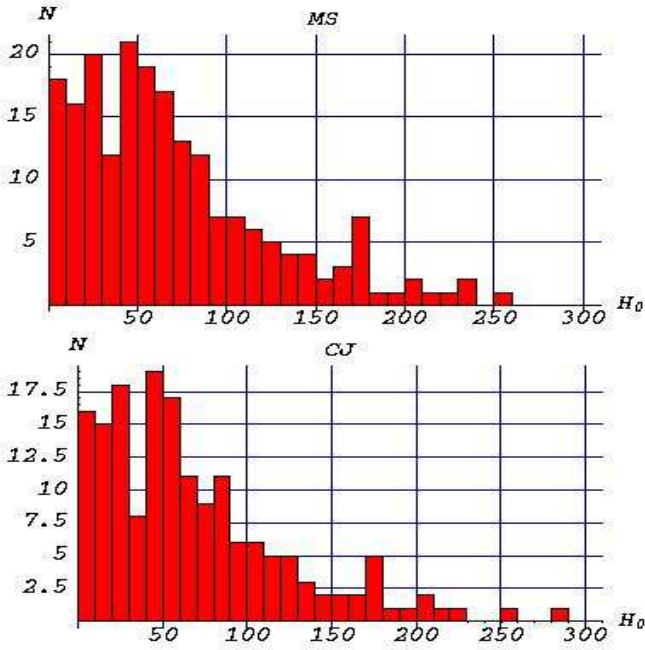


**Figure 30.** A set of calculated, for each source in “all” sample, Hubble constant values (in km/s/Mpc) for  $\bar{\beta}_{\text{“all”}} = 0.987296$  and  $\theta = 8.000265^\circ$  priors derived in a 10 simulations of 1 000 sources for two models MS (top panel) and CJ (bottom panel). Note that (i) the distribution is clearly non-gaussian and the expectation values are greater than the most probable values, and (ii) although these distributions are quite wide, the uncertainty on the expectation value, as calculated according to the method described in Sections 3 and 4, is relatively small.

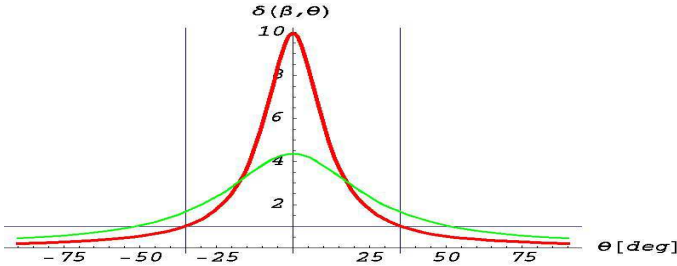


**Figure 31.** The dividing line between a Doppler factor bigger and smaller than one, for some arbitrary value of  $\beta (= 0.98)$  (red line). Any source with such  $\beta$  viewed under angles larger than  $\approx 35^\circ$  would have a Doppler factor less than unity. Other sources (green line) with  $\beta = 0.9$  seen under the same angle would have a bigger Doppler factor.

When dealing with some particular observed Doppler factor distributions, and when performing any analysis on it, the knowledge of any observational selection effect is crucial for having unbiased results. The probability of having biased results also rises with decreasing number of sources. The  $\chi^2$  tests shows, that the flat  $\theta$  distribution is far from being optimal for our samples. This means, that we’re actually dealing with some specially selected sample (which by the way allows to find tight  $\theta$  constraint). In fact, the difference between the

flat case (the simulated flat Doppler distribution) and the best matching model stands for the actual bias effect.

Forcing a minimal Doppler cutoff, although potentially desirable in order to obtain smaller  $\beta$  and  $\theta$  uncertainties, artificially changes the distribution, reduces the number of objects in the sample, and reduces the number of small Doppler values. The latter corresponds to a smaller number of sources with small  $\Xi$  values. This would result in lowering the inferred value of the Hubble constant. Rather than making this somewhat arbitrary forcing of a minimal Doppler cutoff, in this paper we do not present the results for any calculations/simulations made for “geq1” or “geq3” samples.

The  $\beta$  constraint being used is, as described in section 6, the expectancy value of the  $\beta$  PDF, where  $\alpha$  is taken as the mean  $\alpha$  value for the sample, ignoring non-positive spectral indexes, which we consider unphysical. It’s possible that the sources with negative spectral indexes (33% and 32% for the “1st” and “all” samples respectively) present some unusual features in the spectra resulting from eg. non single component mechanism of synchrotron radiation with steep spectrum of Lorentz factor distribution. In this case, under assumption that only the Lorentz factor distributions in jets with steep spectra are reasonable, excluding sources with negative spectral indexes from calculations of  $EX(\beta)$  might help finding a more accurate prior for the whole population of sources, since the sources with positive spectral indexes are still statistically representative part in both samples.

As  $\chi^2$  tests show (eg. Fig. 31) the flat  $\theta$  PDF model cannot reproduce the observed Doppler distribution, as accurately (in terms of estimators introduced in Sec. 6) as some nonuniform, Gaussian-like distribution can. It’s obvious that the parameters of this distribution (Eq. 35) are generally related to the restrictions on the type of sources that are included in analyzed sample. The more restrictive the selection is, the narrower the  $\theta$  distribution should become, however this of course, contradicts having large samples.

When estimating  $\theta$ , we calculate the expectancy value from its modeled (in simulations) distribution function. This allows the estimation of the probability of occurrence of a particular value in terms of confidence levels analysis, which could, in principle, be translated into confidence levels for a Hubble constant estimate. However, as in the case of  $\beta$ , where we do not calculate the most probable value of the distribution, but take its expectancy value, here we also follow this approach, although leaving the confidence levels aside. The choice of using the expectancy values instead of the most probable ones was dictated by the fact, that the grid approach is non smooth and the final results are quantized, just as the grid is. Because the grid was multidimensional, the shape of the fitted  $\theta$  PDF could be altered by  $\sigma$  parameter which possibly could level the impact of non smooth grid. It also accounts for the asymmetry in  $\theta$  PDF due to sharp cut at  $\theta = 0^\circ$ . The full probability analysis would make the uncertainties on the Hubble constant bigger, depending on the applied confidence level. However, since the fitted  $\theta$  PDFs are generally very steep - i.e. have small  $\sigma$  value and often  $n = 4$  - the sizes of uncertainties would be somewhat bigger. For example, for the “all” sample and “grid108” the size of  $H_0$  uncertainty would change from  $\sim 11$  km/s/Mpc

to  $\sim 12$  km/s/Mpc if applied 95 % confidence level in case of “*MS*” model and from  $\sim 15$  km/s/Mpc to  $\sim 29$  km/s/Mpc if 95 % confidence level applied in “*CJ*” case.

## 9. Conclusions

We have shown that, it is relatively straightforward to derive reasonable constraints on the Hubble constant, relying on the VLBI measurements of proper motions of relativistic particles emitting in expanding blobs of plasma within the so called ‘moving sphere’ model of the jet (Ghisellini et al. 1993) (the ‘continuous jet’ model gives similar results). In order to find the constraints on the most crucial (for the calculations) parameters of a jet i.e. the linear velocity of particles in the jet ( $\beta$ ) and the inclination angle ( $\theta$ ), we calculate probability distribution functions (PDFs) on the basis of assumed (within the ‘moving sphere’ model or ‘continuous jet’ model) distribution of Lorentz factors, and derive the expectancy values for  $\beta$  and  $\theta$ . The  $\theta$  estimate is found by varying an ‘a priori’ parametrized  $\theta$  PDF distribution in order to best reproduce the observed Doppler factor distribution. The nonlinear grid of models is calculated and corresponding artificial samples are simulated in order to find the most suitable distribution of inclination angles ( $\varphi_\theta$ ).

The analysis performed on two independent grids in two-fold grid resolution enhancement around preselected areas, provides a good constraint on the Hubble constant. The final value is constrained to be  $H_0 = 71 \pm 7$  km/s/Mpc from the first quality data (“*1st*”) and  $H_0 = 70 \pm 10$  km/s/Mpc from the whole CJF catalog data (“*all*”), for the ‘moving sphere’ model. The final joint Hubble constant value from both samples is constrained to be  $H_0 = 71 \pm 7$  km/s/Mpc (although the uncertainties are probably a bit underestimated because the samples are not entirely independent). The ‘continuous jet’ (“*CJ*”) model implies higher estimates of the Hubble constant, around  $H_0 \sim 94 - 103$  km/s/Mpc, and lower viewing angles, about  $4^\circ$ , though it can be forced to match the ‘moving sphere’ (“*MS*”) model if the viewing angle is forced to higher values. Given that independent constraints on the Hubble constant are much closer to the “*MS*” value, this could be considered evidence in favour of the “*MS*” model for AGN jets (of the class observed in the CJF catalog) and against the “*CJ*” model.

It is important to notice that the accuracy of the  $H_0$  derivations could potentially be substantially improved as the very high resolution space VLBI experiments (like VSOP2 or ARISE) will become operable. This would allow to reduce the proper motion uncertainties that prominently make for the total  $H_0$  uncertainties. In the end, we would like to stress, that the method presented in this paper, somewhat giving very consistent results, could more efficiently be tested using adaptive grid refinement technique, with resolution depending on degree of convergence of reproduced distribution to the observed one. It would also be very interesting either to join or compare the constraints we derived for the viewing angle with those coming from independent methods like morphological, spectral, and/or magnetic field analysis of individual sources. The results of such joint analysis could possibly improve the accuracy and shrink the uncertainties.

*Acknowledgements.* BL would like to thank prof. Ian Browne for bringing his attention to the CJF catalog as a perfect source of useful data for the calculations presented in this paper and also the CJF project Scientific Team for granting him access to these data. SB acknowledges support by the Claussen-Simon-Stiftung.

## References

- Barthel, P. D., Conway, J. E., Myers, S. T., Pearson, T. J., & Readhead, A. C. S. 1995, ApJ, 444, L21
- Barthel, P. D., Pearson, T. J., & Readhead, A. C. S. 1988, ApJ, 329, L51
- Barthel, P. D., Pearson, T. J., Readhead, A. C. S., & Canzian, B. J. 1986, ApJ, 310, L7
- Bennett, C. L., Halpern, M., Hinshaw, G., et al. 2003, ApJS, 148, 1 (arXiv:astro-ph/0302207)
- Biretta, J. A., Moore, R. L., & Cohen, M. H. 1986, ApJ, 308, 93
- Britzen, S., Brinkmann, W., Campbell, R. M., & Vermeulen, R. C. 2005a, A&A submitted
- Britzen, S., Vermeulen, R. C., Campbell, R. M., & Taylor, G. B. 2005b, in prep.
- Britzen, S., Vermeulen, R. C., Taylor, G. B., & Campbell, R. M. 2005c, A&A accepted
- Chodorowski, M. 2004, arXiv:/astro-ph/0407478
- Cohen, M. H., Barthel, P. D., Pearson, T. J., & Zensus, J. A. 1988, ApJ, 329, 1
- Ghisellini, G. 1987, MNRAS, 224, 1
- Ghisellini, G., Padovani, P., Celotti, A., & Maraschi, L. 1993, ApJ, 407, 65
- Gurvits, L. I., Roland, J., Kellermann, K. I., & Frey, S. 1998, in Abstracts of the 19th Texas Symposium on Relativistic Astrophysics and Cosmology, held in Paris, France, Dec. 14-18, 1998. Eds.: J. Paul, T. Montmerle, and E. Aubourg (CEA Saclay), meeting abstract.
- Homan, D. C. & Wardle, J. F. C. 2000, ApJ, 535, 575
- Hough, D. H. & Readhead, A. C. S. 1987, ApJ, 321, L11
- Hough, D. H. & Readhead, A. C. S. 1988, BAAS, 20, 971
- Jones, T. W., O’dell, S. L., & Stein, W. A. 1974, ApJ, 188, 353
- Jorstad, S. G., Marscher, A. P., Mattox, J. R., et al. 2001, ApJSS, 134, 181
- Kellermann, K. I. 1993, Natur, 361, 134
- Koide, S., Nishikawa, K., & Mutel, R. L. 1996, ApJ, 463, L71
- Mastichiadis, A. & Kirk, J. G. 1997, A&A, 320, 19
- Nishikawa, K., Koide, S., Sakai, J., et al. 1997, ApJ, 483, L45
- Nishikawa, K., Koide, S., Sakai, J., et al. 1998, ApJ, 498, 166
- Pearson, T. J., Barthel, P. D., Readhead, A. C. S., & Lawrence, C. R. 1986, in IAU Symp. 119: Quasars, 163+
- Pearson, T. J. & Readhead, A. C. S. 1981, ApJ, 248, 61
- Pearson, T. J., Readhead, C. S., & Barthel, P. D. 1987, in Superluminal Radio Sources, 94–103
- Peebles, P. J. E. 1993, Principles of physical cosmology (Princeton Series in Physics, Princeton, NJ: Princeton University Press, [c1993])
- Pelletier, G. & Roland, J. 1989, A&A, 223, 24
- Spergel, D. N., Verde, L., Peiris, H. V., et al. 2003, ApJS, 148, 175 (arXiv:astro-ph/0302209)
- Stawarz, L., Sikora, M., Ostrowski, M., & Begelman, M. C. 2004, ApJ, 608, 95
- Stern, B. E. & Poutanen, J. 2004, MNRAS, 352, L35
- Taylor, G. B. & Vermeulen, R. C. 1997, ApJ, 485, L9
- Taylor, G. B., Vermeulen, R. C., Readhead, A. C. S., et al. 1996, ApJS, 107, 37

- Ulvestad, J., Johnston, K., Perley, R., & Fomalont, E. 1981, *AJ*, 86, 1010
- Unwin, S. C., Cohen, M. H., Hodges, M. W., Zensus, J. A., & Biretta, J. A. 1989, *ApJ*, 340, 117
- Unwin, S. C., Cohen, M. H., Pearson, T. J., et al. 1983, *ApJ*, 271, 536
- Vermeulen, R. C. & Cohen, M. H. 1994, *ApJ*, 430, 467
- Wehrle, A. E., Cohen, M. H., & Unwin, S. C. 1990, *ApJ*, 351, L1
- Zensus, J. A. & Pearson, T. J. 1988, in *IAU Symp. 129: The Impact of VLBI on Astrophysics and Geophysics*, 7–16